Geophysical Research Letters

RESEARCH LETTER
10.1029/2024GL111150

Special Collection:
Observing CO2 from space: A Decade of progress from NASA's Orbiting Carbon Observatories (OCO-2 and OCO-3)

Estimating Carbon Dioxide Emissions in Two California Cities Using Bayesian Inversion and Satellite Measurements

Sofia D. Hamilton[1], Dien Wu[2], Matthew S. Johnson[3], Alexander J. Turner[4], Marc L. Fischer[1], Nikhil Dadheech[4], and Seongeun Jeong[1]

[1]Energy Analysis and Environmental Impacts Division, Lawrence Berkeley National Laboratory, Berkeley, CA, USA, [2]Division of Geological and Planetary Sciences, California Institute of Technology, Pasadena, CA, USA, [3]Earth Science Division, NASA Ames Research Center, Moffett Field, CA, USA, [4]Department of Atmospheric and Climate Science, University of Washington, Seattle, WA, USA

Abstract NASA's Orbiting Carbon Observatories (OCO-2 and OCO-3) provide measurements of column-averaged carbon dioxide concentrations (XCO_2) with sufficient spatial resolution and precision to constrain bottom-up estimates of CO_2 fluxes at regional scales. We use Bayesian inversion methods assimilating satellite retrievals to improve estimates of CO_2 fluxes in the South Coast Air Basin (SoCAB) which surrounds Los Angeles, and in the San Francisco Bay Area Air Basin (SFBA). We study 2020 to understand the impact of the COVID-19 lockdowns and an active wildfire season. Our results indicated that a 50% (30%) reduction in CO_2 emissions relative to 2015 during the COVID-19 lockdown period was consistent with OCO measurements for SFBA (SoCAB). We find that posterior wildfire emissions differed significantly from the prior at the scale of individual wildfires, though with large uncertainties, and that wildfire emissions in SFBA are significant, attributing 72% of the region's CO_2 emissions during August 2020 to wildfires.

Plain Language Summary Satellites can measure variations in carbon dioxide concentrations over urban areas. These measurements can be combined with models of the atmosphere to validate estimates of carbon dioxide emissions. We use this approach to better understand emissions in and around San Francisco and Los Angeles, the two major cities in California. We study the year 2020 to see how emissions changed in response to COVID-19 lockdowns and to observe emissions from wildfires. The satellite measurements combined with the atmospheric model provide us with updated emission estimates that more closely match the measurements and provide greater certainty than our initial estimate of emissions. We also observe reduced emissions during lockdowns in both cities, updated emissions at the scale of individual wildfires, and large emissions from wildfires during peak wildfire season in the San Francisco Bay Area.

Key Points:

- Satellite measurements can be used to validate emission inventories of CO_2 within urban areas of California
- Changes in CO_2 emissions due to COVID-19 lockdowns and wildfires in 2020 are captured by satellites
- During August 2020, wildfires were responsible for 72% of CO_2 emissions in the Bay Area

Supporting Information:

Supporting Information may be found in the online version of this article.

Correspondence to:

S. D. Hamilton,
sdhamilton@lbl.gov

Citation:

Hamilton, S. D., Wu, D., Johnson, M. S., Turner, A. J., Fischer, M. L., Dadheech, N., & Jeong, S. (2024). Estimating carbon dioxide emissions in two California cities using Bayesian inversion and satellite measurements. *Geophysical Research Letters*, *51*, e2024GL111150. https://doi.org/10.1029/2024GL111150

Received 3 JUL 2024
Accepted 12 OCT 2024

1. Introduction

Urban areas cover only ∼3% of Earth's surface but are responsible for ∼70% of global fossil fuel carbon dioxide (CO_2) emissions (Seto et al., 2014). Accurate emission inventories of greenhouse gases (GHGs) including CO_2 are crucial for ensuring that climate goals are met. Using in situ atmospheric observations to constrain bottom-up emission inventories is important because bottom-up inventories are time-consuming to develop and can have large uncertainties at urban scales, with increasing uncertainty at finer spatial scales (Brophy et al., 2019; Gately & Hutyra, 2017; D. Wu et al., 2018). These inventories often underestimate emissions or have missing sources (Gurney et al., 2021) and can lag several years behind (Roten et al., 2023). Previous studies have used networks of ground-based CO_2 sensors to constrain emissions in urban areas including Los Angeles (Yadav et al., 2021) (LA) and San Francisco (Asimow et al., 2024; Turner et al., 2020a), and subnational regions (Nayagam et al., 2024). Outside of some US cities (e.g., Bares et al., 2019; Davis et al., 2017; Karion et al., 2020; Shusterman et al., 2016; Verhulst et al., 2017), ground-based CO_2 measurement networks are sparse (National Oceanic and Atmospheric Administration: Global Monitoring Laboratory, 2024; D. Wu et al., 2018). However, satellite measurements are now able to characterize GHG emissions not just at the city-scale but even within a city, from space, providing global coverage, a large number of retrievals, and a data set covering many years (D. Wu et al., 2018).

In 2014 NASA launched the Orbiting Carbon Observatory (OCO-2) (Crisp et al., 2008) which collects continuous high-resolution spaceborne measurements of global CO_2 concentrations. Low-Earth orbiting satellites like OCO-2, and OCO-3, retrieve the atmospheric column-averaged dry-air mole fraction of CO_2 (XCO_2). Observations

from these satellites have been used to identify CO_2 enhancements around and within urban areas (Hakkarainen et al., 2016; Kort et al., 2012). New scanning modes, such as OCO-3's Snapshot Area Map (SAM), which was specifically designed to measure anthropogenic emissions, capture a greater spatial region and resolve CO_2 gradients within an urban area (Kiel et al., 2021).

When combined with an atmospheric transport model and emission inventories, these measurements can be used in an inversion framework to constrain emissions. Lagrangian particle dispersion models provide surface influence footprints, which link surface fluxes and measurements of atmospheric CO_2 concentrations. The Column Stochastic Time-Inverted Lagrangian Transport (XSTILT) model is specifically designed for column-averaged satellite measurements (D. Wu et al., 2018). XSTILT has previously been used in conjunction with OCO-2 measurements to constrain city-wide emissions over Riyadh (D. Wu et al., 2018), Lahore (Lei et al., 2021) and the Nile delta region (Shekhar et al., 2020). Observing system simulation experiments (OSSEs) have been used to quantify the ability of satellite measurements to determine true emission fluxes in an inversion framework. These studies generate synthetic satellite measurements from a "true" emission inventory and then use these synthetic measurements and a perturbed emission inventory to estimate the true emission inventory. Previous studies have achieved posterior emissions that are within 7%–30% of the true emissions (Pillai et al., 2016; K. Wu, Palmer, et al., 2023; K. Wu, Yang, et al., 2023). Measurements from OCO-3 are now being used to constrain urban emissions. Roten et al. (2023) used SAM measurements from OCO-3 to constrain CO_2 emissions in LA, separated by source sector, and quantify emissions reductions during the 2020 COVID-19 lockdowns (Roten et al., 2023).

In this study, we use measurements from OCO-2 and OCO-3 in a Bayesian inversion framework to constrain CO_2 fluxes around the San Francisco Bay Area (SFBA) and Los Angeles. To our knowledge, this is the first study to use satellite measurements of CO_2 to constrain emissions in SFBA in an inversion framework. The SFBA is smaller in geographic size and emissions magnitude than megacities like LA, resulting in a smaller signal-to-noise ratio for atmospheric CO_2 measurements needed for inversions. The year 2020 was unusual due to anthropogenic emissions reductions due to the COVID-19 lockdowns (Yañez et al., 2022), large biomass burning emissions due to a particularly active wildfire season (Jerrett et al., 2022; Safford et al., 2022) and severe drought (Steel et al., 2023). These 2020 disruptions to business-as-usual emissions involve atypical changes in emissions in space and time, making them difficult to estimate with bottom-up inventory methods. Satellite measurements can instantly capture the impacts of changing emissions and provide insights into if emissions reductions goals are being met.

2. Methods

We estimate CO_2 fluxes at $0.1° \times 0.1°$ resolution by combing a prior emission inventory and satellite observations in an atmospheric inversion framework. We construct an emission inventory of CO_2 sources (Section 2.1) and use satellite observations to determine urban enhancements and clean background concentrations (Section 2.2). We calculate surface influence footprints that relate surface fluxes to satellite sounding receptors (Section 2.3) and use Bayesian inversion to obtain posterior estimates of fluxes and associated uncertainty (Section 2.4).

2.1. Prior Emission Inventory

Emission inventories were constructed for CO_2 fluxes from the biosphere, fossil fuels and cement production, wildfires, and the ocean. We re-gridded the inventories from their native resolutions to the $0.1° \times 0.1°$ and hourly resolution over our domain, which covers 20°N to 59.9°N and 130°W to 105.1°W. Figure 1 shows annual average CO_2 fluxes from all sources combined.

2.1.1. Fossil Fuels and Cement Production

Fossil fuel CO_2 emission inventories were constructed from a combination of the Vulcan inventory (Gurney et al., 2020a, 2020b) and emission estimates from the California Air Resources Board (CARB) (California Air Resources Board, 2022). The Vulcan inventory (version 3.0) provides a spatially (1 km^2) and temporally (hourly) resolved emission inventory for the entire US, but the most recent year available is 2015. CARB provides an annual emissions total for the entire state through 2021, which is not spatially or temporally resolved. To create a spatially and temporally resolved 2020 inventory, the CARB inventory was used to calculate scaling factors for emissions in 2020 compared to 2015, and the Vulcan inventory was multiplied by these scaling factors (see Table

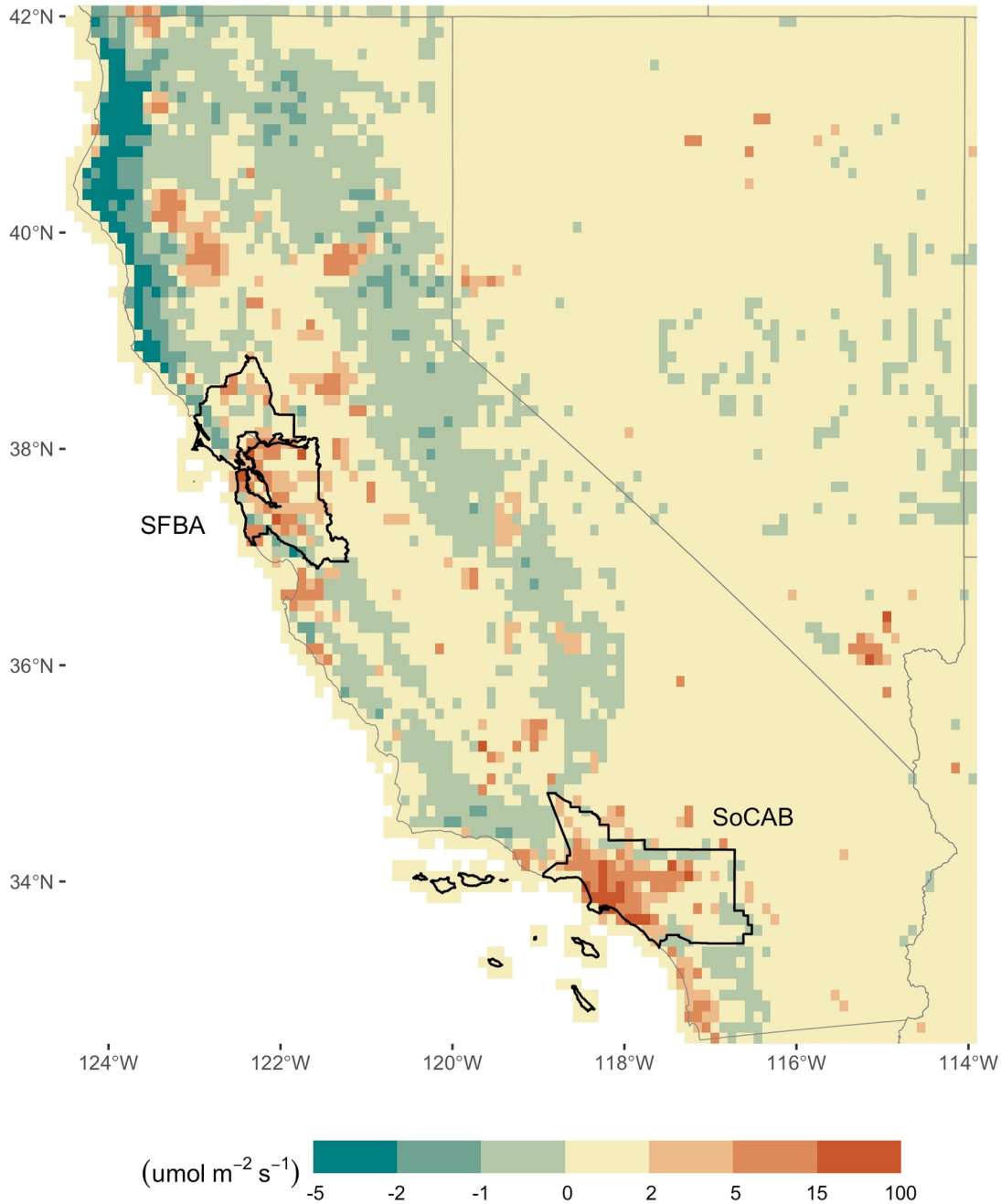

Figure 1. Annual average carbon dioxide emissions (μmol m^{-2} s^{-1}; 0.1° × 0.1°) from the prior emission inventory, overlaid with the CARB-defined San Francisco Bay Area (SFBA) and South Coast (SoCAB) air basins.

S1 in Supporting Information S1). Both Vulcan and CARB provide sector-level emissions estimates, so the scaling was done for each emission sector separately.

Additional monthly scaling factors were applied to sectors most affected by lockdown restrictions (onroad, aviation, and commercial marine vessels), because COVID-19 lockdowns caused emissions to vary widely throughout the year but scaling using the CARB inventory only provides an estimate of the change in total annual emissions. For example, onroad emissions were significantly reduced when lockdowns were first imposed but recovered by the end of 2020 (Harkins et al., 2021; US DOT Federal Highway Administration, 2020). Activity data was used to calculate monthly scaling factors, equal to the ratio of the given month's activity to the annual average. We used vehicle miles traveled in California from the CalTrans Performance Measurement System

(California Department of Transportation, 2022) to estimate activity for the transportation sector. Previous work found that estimations of traffic reductions during the COVID-19 pandemic based on vehicle counts agree well with estimates based on fuel sales (Harkins et al., 2021). For aviation, the number of flights into and out of California from the OpenSky air traffic data set was used (Strohmeier et al., 2021), and for commercial marine vessels, the combined container throughput at the Ports of Oakland, Los Angeles and Long Beach was used (Port of Long Beach, 2022; Port of Oakland, 2022; The Port of Los Angeles, 2022). Scaling factors derived from these data are shown in Table S2 in Supporting Information S1. For all other sectors this ratio is equal to 1.

Emissions for 2020 (V^M_{2020}) are estimated using 2015 Vulcan emissions (V^M_{2015}), the ratio of CARB emissions for 2020 to 2015 for the given sector ($R^{CARB}_{2020/2015}$), and the ratio of monthly activity to annual average activity for the given sector (R^M) as: $V^M_{2020} = V^M_{2015} \cdot R^{CARB}_{2020/2015} \cdot R^M$. This updating of the most recent available inventory (e.g., 2015) was done to ensure that our prior knowledge of emissions was as accurate as possible even before incorporating them into the inversion framework.

2.1.2. Non-Fossil Sources

Ocean fluxes were regridded from the CarbonTracker model (National Oceanic and Atmospheric Administration Global Monitoring Laboratory: Earth System Research Laboratories, 2023). CarbonTracker provides fluxes at $1° \times 1°$ spatial resolution every 3 hours. Wildfire emissions were adapted from a modified Global Fire Emissions Database version 4 (GFED4) which uses MODerate resolution Imaging Spectroradiometer (MODIS) burned area and fire detection data to map wildfire emissions at 500 m resolution (van Wees et al., 2022a).

Fluxes of CO_2 from the biosphere, that is, net ecosystem exchange (NEE), were mapped from the Solar-Induced Fluorescence for Modeling Urban biogenic Fluxes (SMUrF) model (D. Wu et al., 2021a). NEE is the difference between CO_2 release through ecosystem respiration (R_{eco}) and uptake from gross primary production (GPP). The SMUrF model combines space-based measurements of solar-induced fluorescence (a GPP proxy) with eddy-covariance CO_2 flux measurements and machine learning techniques to provide hourly estimates of GPP and R_{eco} that fill in gaps in flux estimates in and around urban areas, at $0.05° \times 0.05°$ resolution. NEE fluxes from this model were evaluated against independent urban eddy-covariance measurements and radiocarbon data (Madsen et al., 2024; D. Wu et al., 2021a; Zazzeri et al., 2023). Previous inversion studies have used this inventory to estimate fluxes from the biosphere (Roten et al., 2023; K. Wu, Palmer, et al., 2023).

2.2. Satellite Observations

We used XCO_2 observations from both OCO-2 and OCO-3 for all of 2020, from nadir and land glint observing modes with good quality flags. We excluded ocean glint observations and overpasses with less than 5 soundings that passed quality check flags. There were no acceptable overpasses for January, so this month was excluded from the analysis.

2.2.1. Filtering and Aggregation

Previous work has shown that even with the bias correction and quality flags implemented by the OCO team, residual biases and noise remain in the OCO retrievals, due to the impacts of aerosols, changing solar and observational geometry, and varying surface properties (Bell et al., 2023; Worden et al., 2017; Wunch et al., 2011). Past studies have employed schemes to filter, bin, and average the soundings before including them in analyses (Crowell et al., 2019; Torres et al., 2019). In order to smooth the noise in the observations and more clearly observe spatial patterns in XCO_2 concentrations we employ the following filtering and aggregation scheme, illustrated in Figures 2a and 2b:

- Step 1 (filtering): OCO measurements were binned by $0.5° \times 0.5°$ latitude and longitude. The mean and standard deviation of each bin was calculated. Any measurements more than two standard deviations from the mean were filtered out. The bins were shifted by 0.25° latitude and longitude, and the filtering was repeated.
- Step 2 (smoothing): A moving average was calculated for each measurement location, defined as the average of all measurements within a 25 km radius of each measurement location.
- Step 3 (aggregation): The smoothed measurements were aggregated into bins of $0.1° \times 0.1°$ latitude and longitude.

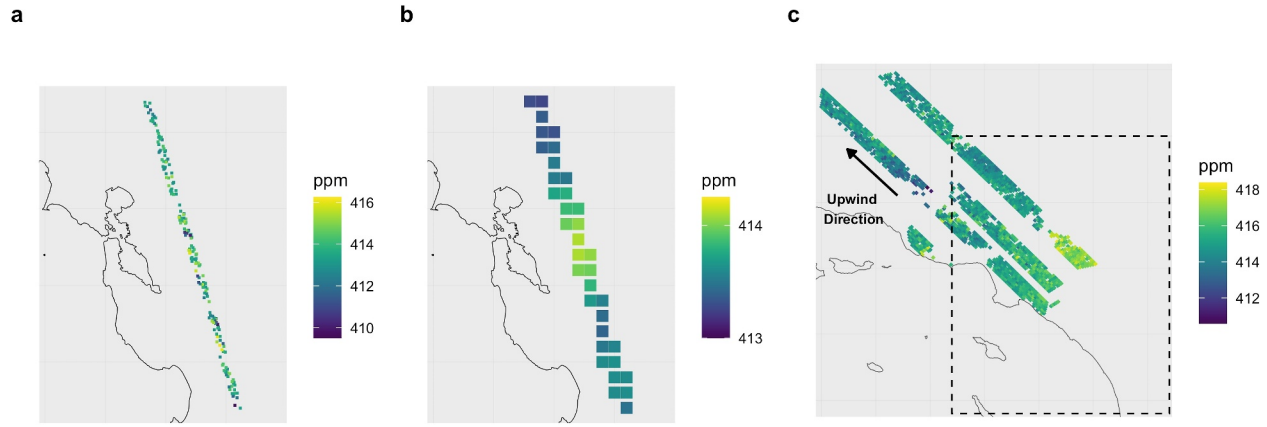

Figure 2. Example of OCO measurements (ppm) used in filtering/aggregation and defining background concentrations. (a) OCO-2 bias-corrected XCO_2 measurements near the SFBA domain on 10 February 2020 with good quality flag. (b) Aggregated XCO_2 measurements from panel (a), after filtering and averaging. Note the reduced range of the color scale. (c) OCO-3 XCO_2 soundings from 31 July 2020 in the SOCAB region. The soundings outside the inversion domain (dashed line box) are averaged to define the background concentration for soundings inside the inversion domain.

The second filtering step was determined to be necessary because with only one filter pass, it was possible for extreme OCO observation values to end up in their own bin and escape filtering, resulting in highly variable pixel-to-pixel values which are not physically realistic. Two filtering steps were preferable to setting a minimum number of measurements needed per bin because this alternative would risk removing reasonable values near the edges of the OCO swath. The filtering, smoothing, and aggregation illuminate general spatial patterns in XCO_2 concentrations while reducing the impacts of noise. Though it is not mathematically necessary for the observations to match the emission/footprint grid resolution, since we cannot resolve fine-scale details at the level of individual soundings within each grid cell, the aggregation allows us to assimilate one representative value per cell (Crowell et al., 2019).

2.2.2. Background Concentrations

Obtaining an accurate estimate of the background concentration is crucial for inferring emissions using inverse modeling, since we are interested in the concentration *enhancement* above background due to emissions within our inversion domain. Column enhancements over Los Angeles range from 0 to 6 ppm with a median enhancement of 2 ppm (Kiel et al., 2021), while total XCO_2 exceeds 400 ppm. Around SFBA, enhancements are smaller, since emissions there are less than in LA (see Figure 1). An error in the estimated background concentration of just 1 ppm could potentially cancel out the entire concentration enhancement, despite being a relatively small fractional error in total background concentration. To ensure consistency between estimated background concentrations and measured enhancements, OCO observations were used to define clean background concentrations. Particle trajectories from XSTILT runs were used to observe the upwind direction for each overpass. If the OCO overpass included measurements outside the urban area in this upwind region, the average of those measurements was used as the background concentration. Figure 2c shows an example of this case. When upwind measurements were not available, OCO measurements over locations with modeled fossil fuel enhancements of less than 0.05 ppm were used. If no OCO measurements of this type were available, the background measurements from the nearest (in time) overpass were used. About 71% of overpasses had measurements from the same day that could define the background concentration and about 20% used measurements from within one to 7 days. Similar methods have been used previously for establishing clean background using satellite measurements (Janardanan et al., 2016; D. Wu et al., 2018).

2.3. Surface Influence Footprints

The XSTILT model was used to calculate surface influence footprints that relate surface fluxes with concentration enhancements in the OCO soundings. Meteorology from the Weather Research and Forecasting model (Skamarock et al., 2021) was used to drive the XSTILT simulations. The meteorological modeling and evaluation are described in the Section S1.1 in Supporting Information S1.

The XSTILT model was run for each sounding with a "good" quality flag in every OCO-2 and OCO-3 overpass in 2020. XSTILT was run backward in time for 5 days, obtaining hourly surface influence footprints for each sounding at $0.1° \times 0.1°$ spatial resolution. These footprints were then convolved with the hourly emission inventories to generate predicted XCO_2 enhancements for each OCO sounding. For our inversion application, footprints were calculated over the inversion domain for SFBA or SoCAB, to calculate only the XCO_2 enhancement due to emissions within our inversion domain.

2.4. Bayesian Inversion

2.4.1. Posterior Fluxes

A Bayesian inversion was used to obtain posterior CO_2 fluxes at hourly resolution for each grid cell within our domain. Posterior fluxes ($\hat{\mathbf{x}}$) were calculated from prior fluxes ($\mathbf{x_a}$), the surface influence footprint matrix ($\mathbf{H}$), the prior error covariance matrix ($\mathbf{B}$), the model-data mismatch error covariance matrix ($\mathbf{R}$) and measurements ($\mathbf{y}$), as shown in Equation 1.

$$\hat{\mathbf{x}} = \mathbf{x_a} + (\mathbf{HB})^{\mathrm{T}}\left(\mathbf{HBH}^{\mathrm{T}} + \mathbf{R}\right)^{-1}(\mathbf{y} - \mathbf{Hx_a}) \quad (1)$$

The inversion was implemented by adapting the method from Turner et al. (2020a). Following Yadav and Michalak (2013), the prior error covariance matrix was treated as a separable Kronecker product of the spatial and temporal error covariance matrices, in order to improve computational efficiency. The model-data mismatch error covariance matrix ($\mathbf{R}$) includes instrument error, background error, and model error, which are added in quadrature. The instrument error was taken from the XCO_2 uncertainty reported in the OCO measurements for each sounding. The reported uncertainty is the posterior uncertainty for the retrieval, including measurement error, smoothing error, interference error, and forward model error (C. W. O'Dell et al., 2012). Instrument errors were added in quadrature for aggregation. The average instrument error across all soundings was 1.03 ppm. Background error was taken from the standard deviation of the OCO measurements used to define the background concentration for that sounding. Since the background concentration and error are the same for all soundings in a given overpass, this error was not aggregated, but simply assigned to the aggregated sounding. The average background error was 1.19 ppm. For model error, we use a combination of stochastic model error (0.06 ppm), boundary layer height error (0.20 ppm), and horizontal wind error (1.00), added in quadrature (D. Wu et al., 2018). For the prior emissions we assume 50% uncertainty on the total CO_2 emissions.

2.4.2. Posterior Covariance

The posterior covariance ($\mathbf{V_{\hat{s}}}$) is calculated from the surface influence footprint matrix ($\mathbf{H}$), the prior error covariance matrix ($\mathbf{B}$), and the model-data mismatch error covariance matrix ($\mathbf{R}$), following Equation 2. This method was adapted from Yadav and Michalak to directly calculate posterior covariance for each grid cell on aggregated (monthly) time scales (Yadav & Michalak, 2013). This results in significant computational cost and memory savings over calculating posterior covariance for each hour and then aggregating.

$$\mathbf{V_{\hat{s}}} = \mathbf{B} - (\mathbf{HB})^{\mathrm{T}}\left(\mathbf{HBH}^{\mathrm{T}} + \mathbf{R}\right)^{-1}\mathbf{HB} \quad (2)$$

3. Results

3.1. Prior and Posterior Column Enhancements

The inversion was conducted for each domain for each month of 2020 (excluding January for which no acceptable observations were available). The resulting posterior fluxes were used to calculate updated predicted column enhancements (i.e., concentrations; see Figures S5–S8 in Supporting Information S1) for the receptors used in the inversion. These were compared to the measured enhancements from OCO, as well as the predictions using the prior fluxes. Including the entire year of soundings, the RMSE was reduced by 16% and 32% and the correlation coefficient was increased by 44% and 30% in the SFBA and SoCAB domains, respectively. Though we cannot validate the inversion with these assimilated observations, this result suggests that the posterior fluxes from our inversions are more aligned with the observations than the prior estimates.

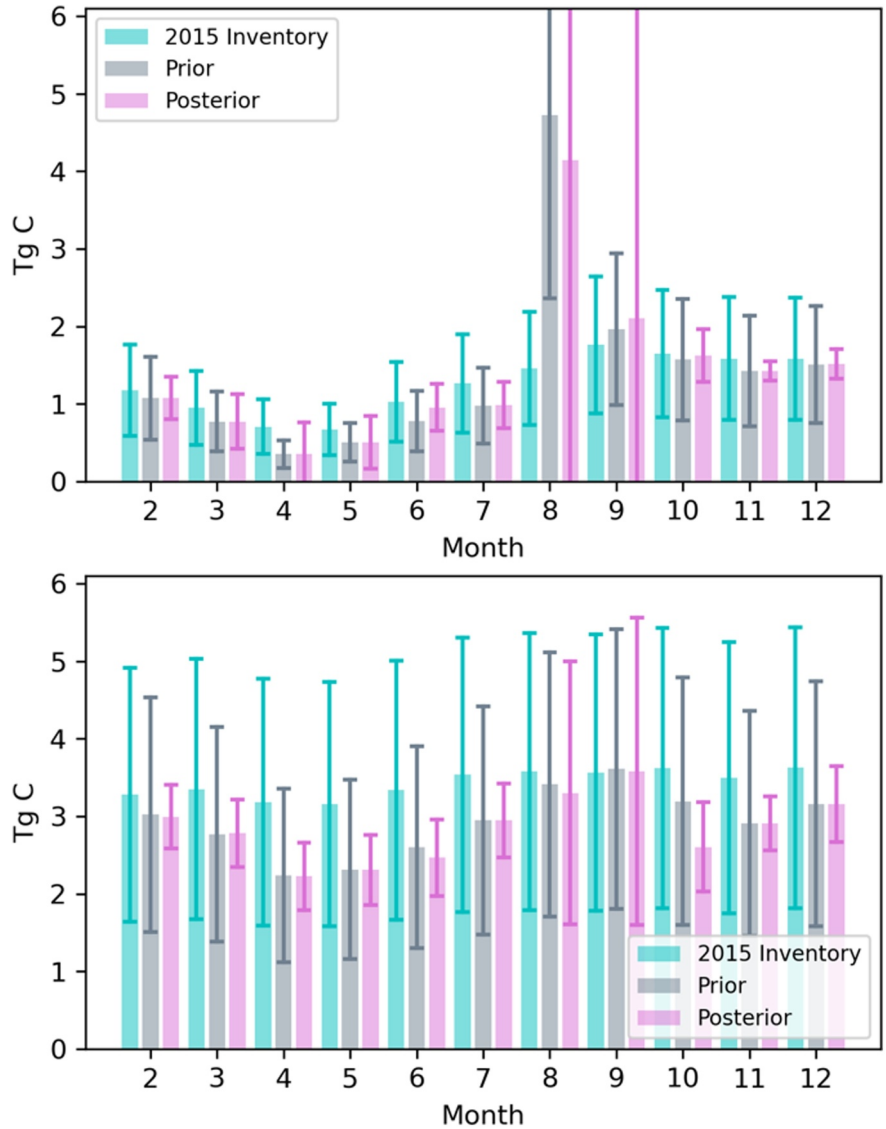

Figure 3. Total CO_2 emissions (Tg C month^{-1}) in SFBA (top) and SoCAB (bottom) for 2015 inventory, prior 2020 inventory, and posterior 2020 estimates, including uncertainty bars (one standard deviation). The error bars for the 2020 prior and the 2015 inventory assume 50% uncertainty.

3.2. Satellite Constraints on Total Emissions for Each Air Basin

Total prior and posterior emissions, and associated uncertainty, were calculated for the CARB-defined air basin corresponding to each urban area: San Francisco Bay Air Basin (SFBA) and South Coast Air Basin (SoCAB). Air basin outlines are shown in Figure 1. Generally, the total emissions were similar between the prior and posterior, and the uncertainties were reduced in the posterior estimates. Past studies have used the Vulcan data for the year 2015 as the prior, and thus see larger deviations in the posterior (Roten et al., 2023; Yadav et al., 2021). Other studies validated the patterns in time in the posterior emissions in 2020 against activity data (Roten et al., 2023), while we adjusted the prior before inversions. Consequently, even the enhancements predicted from our prior emission inventory have good agreement with observations, and deviations from the prior are not so large. To test that this is the case, we ran four months of the inversion using 2015 fossil fuel emissions in the prior, and we observe larger changes between the prior and posterior, particularly in SoCAB where there are more observations available to constrain fluxes, see Figure S9 in Supporting Information S1.

Figure 3 compares the total monthly prior and posterior emissions, as well as 2015 emissions. The 2015 inventory is the sum of the 2015 Vulcan fossil fuel emissions (Gurney et al., 2020a, 2020b), SMUrF NEE fluxes (D. Wu et al., 2021a), and fire emissions from CarbonTracker (National Oceanic and Atmospheric Administration Global Monitoring Laboratory: Earth System Research Laboratories, 2023). Note that the adaptation of the prior using the 2020 activity data results in large changes from the 2015 inventory, which are consistent in the posterior. The impact of the lockdowns can be clearly seen in the posterior compared to 2015. For example, in April 2020, at the height of the lockdown, emissions are reduced by 50% and 30% compared to 2015 in SFBA and SoCAB, respectively. A notable exception to the consistency between our prior and posterior is during wildfire events in SFBA in August and September, where more noticeable changes between the prior and posterior were found, and posterior uncertainty was increased. The fires emitted huge quantities of CO_2, dwarfing emissions in any other month. In August, when the wildfires were active in SFBA, wildfire emissions account for about 72% of total monthly CO_2 emissions in SFBA.

These very large emissions are sporadic and co-emitted with aerosols, leading to limited observational coverage from space which contributes to the large uncertainty. When observations are few or there is a discrepancy between the prior fluxes and observations, the posterior uncertainty can be larger than prior uncertainty (Euskirchen et al., 2022; van de Schoot et al., 2014). The SoCAB domain typically has more observations than SFBA, resulting in relatively smaller posterior uncertainties, and posterior uncertainty that is smaller than prior uncertainty in all non-wildfire months. This underscores the value of these observations, which will be increasingly important for validating emissions as more satellites are launched and more observations are acquired. Figure S9 in Supporting Information S1, which compares four months of the inversion using 2015 fossil fuel emissions in the prior, also illustrates how the posterior uncertainty is larger for the prior with 2015 emissions than the prior with 2020 emissions (when there is a larger discrepancy between the prior and the observations), highlighting the importance of the emissions scaling in order to obtain as accurate a prior as possible, and thus reduce posterior uncertainty.

These results indicate that challenges still exist with satellite observations during large wildfires, and sparsely-observed urban areas, highlighting the need for further research to address these uncertainties. In terms of the annual (excluding January) totals, our mean posterior emissions were reduced by 1% and 3% compared to the priors in SFBA and SoCAB, respectively. In SoCAB (SFBA), our prior Feb-Dec total of 32.2 ± 16.1 (15.6 ± 7.8) Tg C was reduced to 31.3 ± 3.0 (15.5 ± 35.5) Tg C. As discussed, the large wildfires in SFBA introduce very large posterior uncertainties.

3.3. Wildfire Emissions

The posterior emissions show noticeable changes to emissions within the wildfire boundaries in SFBA, as shown in Figure S10 in Supporting Information S1. OCO overpasses during fire season were sensitive to wildfire emissions, with modeled XCO_2 enhancements from fires as high as ~0.35 ppm. However, these overpasses had fewer retrievals with good quality flags, likely due to the influence of aerosols present in wildfire smoke. Figure S11 in Supporting Information S1 shows an example of an overpass with sensitivity to wildfire emissions during wildfire activity, where the surface influence footprint covers the fire area. Our posterior emissions show that the prior inventory overpredicted wildfire emissions, though the uncertainty on emissions in these wildfire grid cells is large (see Table S5 in Supporting Information S1). In general, the presence of large emissions due to wildfires is associated with increased posterior uncertainty throughout our domain, especially in grid cells containing wildfires. Figures S12 and S13 in Supporting Information S1 demonstrate the difference in posterior uncertainty for an active fire month (August) and non-fire month (December). This suggests that OCO can provide useful information about the central estimates for wildfire emissions, but that the uncertainty associated with those estimates pose challenges for inverse modeling using OCO data, especially for this type of high-resolution, pixel-based inversion with a large number of parameters. Source inversion with only a few parameters (i.e., one scaling factor for each source sector) maybe be useful to reduce uncertainty. This challenge is partially due to the fact that there are not many other observations that can constrain suburban wildfire emissions. One previous study examining the southwestern US found large carbon losses from the terrestrial biosphere due to wildfires in 2020 using OCO-2 measurements (Chen et al., 2024), but future studies are needed to better understand the ability of OCO data to constrain fire emissions at higher spatial resolution. Wildfires were also present in our SoCal domain, with smaller emissions magnitudes but still large uncertainty (see Figure S14 and Table S5 in Supporting Information S1).

4. Conclusions and Discussion

NASA's OCO-2 and OCO-3 satellites are useful for validating updated emission inventories at urban scales. Satellite measurements can help identify sporadic sources that threaten progress in emissions reductions, such as emissions from wildfires. Although we found large uncertainties in wildfire grid cells within our domain, a future with more frequent satellite measurements over large wildfires could help reduce this uncertainty and better understand sources like wildfires that are becoming increasingly important in our changing climate, as well as smaller cities like San Francisco which have not yet been a focus area for satellite observations. The posterior inventory from this study is validated by close agreement with the results found in Yadav et al. (2021), with differences in monthly CO_2 emissions in the South Coast Air Basin between these two studies within 6%–17% (see Figure S15 in Supporting Information S1). Multiple studies have now observed the impacts of the COVID-19 lockdowns in Los Angeles on emissions using satellite data (Roten et al., 2023; Yadav et al., 2021). This study adds to this body of work by using similar methods to observe emissions in the San Francisco Bay Area. Previous studies up until this point have generally focused on megacities, but these results indicate that these newer scanning modes can be useful for smaller cities, as more data becomes available. As more of these satellites are launched and more data is collected, this methodology can be used more widely to validate emissions estimates more quickly than with bottom-up estimates.

Data Availability Statement

OCO-3 Level 2 v10.4r and OCO-2 Level 2 v11r data are available from (NASA EarthData, 2024). Vulcan version 3.0 data set is available at (Gurney et al., 2020a, 2020b). The CARB GHG Emission inventory is available at (California Air Resources Board, 2022). CalTrans PeMS data is available at (California Department of Transportation, 2022). OpenSky Network data is available at (Olive et al., 2022). Container throughput counts are available for the Port of Oakland at (Port of Oakland, 2022), Port of Los Angeles at (The Port of Los Angeles, 2022), and Port of Long Beach at (Port of Long Beach, 2022). CarbonTracker fluxes are available from (NOAA Global Monitoring Laboratory, 2024). SMUrF model data are available from (D. Wu et al., 2021b). Fire emissions data is available from (van Wees et al., 2022b). The inversion code is available at (Turner et al., 2020b). Posterior covariance code is available from the Supplement at (Yadav & Michalak, 2013).

Acknowledgments
Work at Lawrence Berkeley National Laboratory (LBNL) was supported by NASA's funding (*80HQTR21T0101*) through the Carbon Cycle Science Program, under Contract No. DE-AC02-05CH11231 with the U.S. Department of Energy. The authors thank the PI Computing Allowance Program at LBNL for computing allocations from the Lawrencium Cluster to conduct this work. Additional computing resources supporting this work were provided by the NASA High-End Computing Program through the NASA Advanced Supercomputing Division at NASA Ames Research Center. The views and opinions expressed herein by the authors do not necessarily state or reflect those of NASA, the United States Government, or the Regents of the University of California.

References

Asimow, N. G., Turner, A. J., & Cohen, R. C. (2024). Sustained reductions of Bay area CO2 emissions 2018–2022. *Environmental Science & Technology*, *58*(15), 6586–6594. https://doi.org/10.1021/acs.est.3c09642

Bares, R., Mitchell, L., Fasoli, B., Bowling, D. R., Catharine, D., Garcia, M., et al. (2019). The Utah urban carbon dioxide (UUCON) and Uintah basin greenhouse gas networks: Instrumentation, data, and measurement uncertainty. *Earth System Science Data*, *11*(3), 1291–1308. https://doi.org/10.5194/essd-11-1291-2019

Bell, E., O'Dell, C. W., Taylor, T. E., Merrelli, A., Nelson, R. R., Kiel, M., et al. (2023). Exploring bias in the OCO-3 snapshot area mapping mode via geometry, surface, and aerosol effects. *Atmospheric Measurement Techniques*, *16*(1), 109–133. https://doi.org/10.5194/amt-16-109-2023

Brophy, K., Graven, H., Manning, A. J., White, E., Arnold, T., Fischer, M. L., et al. (2019). Characterizing uncertainties in atmospheric inversions of fossil fuel CO2 emissions in California. *Atmospheric Chemistry and Physics*, *19*(5), 2991–3006. https://doi.org/10.5194/acp-19-2991-2019

California Air Resources Board. (2022). Current California GHG emission inventory data [Dataset]. https://ww2.arb.ca.gov/ghg-inventory-data

California Department of Transportation. (2022). CalTrans performance measurement system [Dataset]. https://pems.dot.ca.gov/

Chen, H., He, W., Liu, J., Nguyen, N. T., Chevallier, F., Yang, H., et al. (2024). Satellite-detected large CO_2 release in southwestern North America during the 2020–2021 drought and associated wildfires. *Environmental Research Letters*, *19*(5), 054047. https://doi.org/10.1088/1748-9326/ad3cf7

Crisp, D., Miller, C. E., & DeCola, P. L. (2008). NASA orbiting carbon observatory: Measuring the column averaged carbon dioxide mole fraction from space. *Journal of Applied Remote Sensing*, *2*(1), 023508. https://doi.org/10.1117/1.2898457

Crowell, S., Baker, D., Schuh, A., Basu, S., Jacobson, A. R., Chevallier, F., et al. (2019). The 2015–2016 carbon cycle as seen from OCO-2 and the global in situ network. *Atmospheric Chemistry and Physics*, *19*(15), 9797–9831. https://doi.org/10.5194/acp-19-9797-2019

Davis, K. J., Deng, A., Lauvaux, T., Miles, N. L., Richardson, S. J., Sarmiento, D. P., et al. (2017). The Indianapolis Flux experiment (INFLUX): A test-bed for developing urban greenhouse gas emission measurements. *Elementa: Science of the Anthropocene*, *5*. https://doi.org/10.1525/elementa.188

Euskirchen, E. S., Bruhwiler, L. M., Commane, R., Parmentier, F.-J. W., Schädel, C., Schuur, E. A. G., & Watts, J. (2022). Current knowledge and uncertainties associated with the Arctic greenhouse gas budget. In *Balancing greenhouse gas budgets* (pp. 159–201). Elsevier. https://doi.org/10.1016/B978-0-12-814952-2.00007-1

Gately, C. K., & Hutyra, L. R. (2017). Large uncertainties in urban-scale carbon emissions. *Journal of Geophysical Research: Atmospheres*, *122*(20). https://doi.org/10.1002/2017JD027359

Gurney, K. R., Liang, J., Patarasuk, R., Song, Y., Huang, J., & Roest, G. (2020a). Vulcan: High-Resolution hourly fossil fuel CO2 emissions in USA, 2010-2015, *version 3* [Dataset]. https://doi.org/10.3334/ORNLDAAC/1810

Gurney, K. R., Liang, J., Patarasuk, R., Song, Y., Huang, J., & Roest, G. (2020b). The Vulcan version 3.0 high-resolution fossil fuel CO_2 emissions for the United States. *Journal of Geophysical Research: Atmospheres*, *125*(19). https://doi.org/10.1029/2020JD032974

Gurney, K. R., Liang, J., Roest, G., Song, Y., Mueller, K., & Lauvaux, T. (2021). Under-reporting of greenhouse gas emissions in U.S. cities. *Nature Communications*, *12*(1), 553. https://doi.org/10.1038/s41467-020-20871-0

Hakkarainen, J., Ialongo, I., & Tamminen, J. (2016). Direct space-based observations of anthropogenic CO2 emission areas from OCO-2. *Geophysical Research Letters*, *43*(21). https://doi.org/10.1002/2016GL070885

Harkins, C., McDonald, B. C., Henze, D. K., & Wiedinmyer, C. (2021). A fuel-based method for updating mobile source emissions during the COVID-19 pandemic. *Environmental Research Letters*, *16*(6), 065018. https://doi.org/10.1088/1748-9326/ac0660

Janardanan, R., Maksyutov, S., Oda, T., Saito, M., Kaiser, J. W., Ganshin, A., et al. (2016). Comparing GOSAT observations of localized CO $_2$ enhancements by large emitters with inventory-based estimates. *Geophysical Research Letters*, *43*(7), 3486–3493. https://doi.org/10.1002/2016GL067843

Jerrett, M., Jina, A. S., & Marlier, M. E. (2022). Up in smoke: California's greenhouse gas reductions could be wiped out by 2020 wildfires. *Environmental Pollution*, *310*, 119888. https://doi.org/10.1016/j.envpol.2022.119888

Karion, A., Callahan, W., Stock, M., Prinzivalli, S., Verhulst, K. R., Kim, J., et al. (2020). Greenhouse gas observations from the Northeast Corridor tower network. *Earth System Science Data*, *12*(1), 699–717. https://doi.org/10.5194/essd-12-699-2020

Kiel, M., Eldering, A., Roten, D. D., Lin, J. C., Feng, S., Lei, R., et al. (2021). Urban-focused satellite CO2 observations from the orbiting carbon observatory-3: A first look at the Los Angeles megacity. *Remote Sensing of Environment*, *258*, 112314. https://doi.org/10.1016/j.rse.2021.112314

Kort, E. A., Frankenberg, C., Miller, C. E., & Oda, T. (2012). Space-based observations of megacity carbon dioxide. *Geophysical Research Letters*, *39*(17). https://doi.org/10.1029/2012GL052738

Lei, R., Feng, S., Danjou, A., Broquet, G., Wu, D., Lin, J. C., et al. (2021). Fossil fuel CO2 emissions over metropolitan areas from space: A multi-model analysis of OCO-2 data over Lahore, Pakistan. *Remote Sensing of Environment*, *264*, 112625. https://doi.org/10.1016/j.rse.2021.112625

Madsen, S., Wu, D., Halim, M. A., & Wunch, D. (2024). CO2 fluxes of vegetation in the Greenbelt of Ontario and increased net ecosystem emissions associated with its removal. *Elem Sci Anth*, *12*(1). https://doi.org/10.1525/elementa.2023.00102

NASA EarthData. (2024). GES DISC [Dataset]. https://disc.gsfc.nasa.gov/

National Oceanic and Atmospheric Administration Global Monitoring Laboratory. (2023). Earth system research Laboratories. *CarbonTracker CT2022*. Retrieved from https://gml.noaa.gov/ccgg/carbontracker/

National Oceanic and Atmospheric Administration: Global Monitoring Laboratory. (2024). In-situ measurement program. Retrieved from https://gml.noaa.gov/ccgg/insitu/#:~:text=NOAA%20Baseline%20Observatories&text=GML%20measures%20greenhouse%20gases%20at,CO%20measurements%20in%20the%201980's

Nayagam, L., Maksyutov, S., Oda, T., Janardanan, R., Trisolino, P., Zeng, J., et al. (2024). A top-down estimation of subnational CO2 budget using a global high-resolution inverse model with data from regional surface networks. *Environmental Research Letters*, *19*(1), 014031. https://doi.org/10.1088/1748-9326/ad0f74

NOAA Global Monitoring Laboratory. (2024). CarbonTracker [Dataset]. https://gml.noaa.gov/aftp/products/carbontracker/co2/CT-NRT.v2022-1/fluxes/daily/

O'Dell, C. W., Connor, B., Bosch, H., O'Brien, D., Frankenberg, C., Castano, R., et al. (2012). The ACOS CO2 retrieval algorithm – Part 1: Description and validation against synthetic observations. *Atmospheric Measurement Techniques*, *5*(1), 99–121. https://doi.org/10.5194/amt-5-99-2012

Olive, X., Strohmeier, M., & Lübbe, J. (2022). Crowdsourced air traffic data from the OpenSky Network 2020 [Dataset]. https://doi.org/10.5281/zenodo.3931948

Pillai, D., Buchwitz, M., Gerbig, C., Koch, T., Reuter, M., Bovensmann, H., et al. (2016). Tracking city CO2 emissions from space using a high-resolution inverse modelling approach: A case study for Berlin, Germany. *Atmospheric Chemistry and Physics*, *16*(15), 9591–9610. https://doi.org/10.5194/acp-16-9591-2016

Port of Long Beach. (2022). TEUs archive: 1987 to present by month [Dataset]. https://polb.com/business/port-statistics/#teus-archive-1995-to-present

Port of Oakland. (2022). Facts & Figures [Dataset]. https://www.oaklandseaport.com/performance/facts-figures/

Roten, D., Lin, J. C., Das, S., & Kort, E. A. (2023). Constraining sector-specific CO2 fluxes using space-based XCO2 observations over the Los Angeles basin. *Geophysical Research Letters*, *50*(21). https://doi.org/10.1029/2023GL104376

Safford, H. D., Paulson, A. K., Steel, Z. L., Young, D. J. N., & Wayman, R. B. (2022). The 2020 California fire season: A year like no other, a return to the past or a harbinger of the future? *Global Ecology and Biogeography*, *31*(10), 2005–2025. https://doi.org/10.1111/geb.13498

Seto, K. C., Dhakal, S., Bigio, A., Blanco, H., D'elgado, G., Dewar, D., et al. (2014). Human settlements, infrastructure, and spatial planning. In *Climate change 2014: Mitigation of climate change. Contribution of working group III to the fifth assessment report of the intergovernmental panel on climate change*.

Shekhar, A., Chen, J., Paetzold, J. C., Dietrich, F., Zhao, X., Bhattacharjee, S., et al. (2020). Anthropogenic CO2 emissions assessment of Nile Delta using XCO2 and SIF data from OCO-2 satellite. *Environmental Research Letters*, *15*(9), 095010. https://doi.org/10.1088/1748-9326/ab9cfe

Shusterman, A. A., Teige, V. E., Turner, A. J., Newman, C., Kim, J., & Cohen, R. C. (2016). The BErkeley atmospheric CO2 observation network: Initial evaluation. *Atmospheric Chemistry and Physics*, *16*(21), 13449–13463. https://doi.org/10.5194/acp-16-13449-2016

Skamarock, W. C., Klemp, J. B., Dudhia, J., Gill, D. O., Liu, Z., Berner, J., et al. (2021). A description of the advanced research WRF model version 4.3.

Steel, Z. L., Jones, G. M., Collins, B. M., Green, R., Koltunov, A., Purcell, K. L., et al. (2023). Mega-disturbances cause rapid decline of mature conifer forest habitat in California. *Ecological Applications*, *33*(2). https://doi.org/10.1002/eap.2763

Strohmeier, M., Olive, X., Lübbe, J., Schäfer, M., & Lenders, V. (2021). Crowdsourced air traffic data from the OpenSky Network 2019–2020. *Earth System Science Data*, *13*(2), 357–366. https://doi.org/10.5194/essd-13-357-2021

The Port of Los Angeles. (2022). Container statistics [Dataset]. https://www.portoflosangeles.org/business/statistics/container-statistics

Torres, A. D., Keppel-Aleks, G., Doney, S. C., Fendrock, M., Luis, K., De Mazière, M., et al. (2019). A geostatistical framework for quantifying the imprint of mesoscale atmospheric transport on satellite trace gas retrievals. *Journal of Geophysical Research: Atmospheres*, *124*(17–18), 9773–9795. https://doi.org/10.1029/2018JD029933

Turner, A. J., Kim, J., Fitzmaurice, H., Newman, C., Worthington, K., Chan, K., et al. (2020a). Observed impacts of COVID-19 on urban CO2 emissions. *Geophysical Research Letters*, *47*(22). https://doi.org/10.1029/2020GL090037

Turner, A. J., Kim, J., Fitzmaurice, H., Newman, C., Worthington, K., Chan, K., et al. (2020b). UrbanInversion [Software]. https://github.com/alexjturner/UrbanInversion

US DOT Federal Highway Administration. (2020). Traffic volume trends. Retrieved from https://www.Fhwa.Dot.Gov/Policyinformation/Travel_monitoring/Tvt.Cfm

van de Schoot, R., Kaplan, D., Denissen, J., Asendorpf, J. B., Neyer, F. J., & van Aken, M. A. G. (2014). A gentle introduction to Bayesian analysis: Applications to developmental research. *Child Development*, *85*(3), 842–860. https://doi.org/10.1111/cdev.12169

van Wees, D., van der Werf, G. R., Randerson, J. T., Rogers, B. M., Chen, Y., Veraverbeke, S., et al. (2022a). Global biomass burning fuel consumption and emissions at 500 m spatial resolution based on the Global Fire Emissions Database (GFED). *Geoscientific Model Development*, *15*(22), 8411–8437. https://doi.org/10.5194/gmd-15-8411-2022

van Wees, D., van der Werf, G. R., Randerson, J. T., Rogers, B. M., Chen, Y., Veraverbeke, S., et al. (2022b). *Model data for 'Global biomass burning fuel consumption and emissions at 500-m spatial resolution based on the Global Fire Emissions Database (GFED)'* [Dataset]. https://doi.org/10.5281/zenodo.7229674

Verhulst, K. R., Karion, A., Kim, J., Salameh, P. K., Keeling, R. F., Newman, S., et al. (2017). Carbon dioxide and methane measurements from the Los Angeles megacity carbon project – Part 1: Calibration, urban enhancements, and uncertainty estimates. *Atmospheric Chemistry and Physics*, *17*(13), 8313–8341. https://doi.org/10.5194/acp-17-8313-2017

Worden, J. R., Doran, G., Kulawik, S., Eldering, A., Crisp, D., Frankenberg, C., et al. (2017). Evaluation and attribution of OCO-2 XCO2 uncertainties. *Atmospheric Measurement Techniques*, *10*(7), 2759–2771. https://doi.org/10.5194/amt-10-2759-2017

Wu, D., Lin, J. C., Duarte, H. F., Yadav, V., Parazoo, N. C., Oda, T., & Kort, E. A. (2021a). A model for urban biogenic CO2 fluxes: Solar-induced fluorescence for modeling urban biogenic fluxes (SMUrF v1). *Geoscientific Model Development*, *14*(6), 3633–3661. https://doi.org/10.5194/gmd-14-3633-2021

Wu, D., Lin, J. C., Duarte, H. F., Yadav, V., Parazoo, N. C., Oda, T., & Kort, E. A. (2021b). wde0924/SMUrF: SMUrF v1 for GMD submission [Dataset]. https://doi.org/10.5281/zenodo.4018123

Wu, D., Lin, J. C., Fasoli, B., Oda, T., Ye, X., Lauvaux, T., et al. (2018). A Lagrangian approach towards extracting signals of urban CO2 emissions from satellite observations of atmospheric column CO2 (XCO2): X-stochastic time-inverted Lagrangian transport model ("X-STILT v1"). *Geoscientific Model Development*, *11*(12), 4843–4871. https://doi.org/10.5194/gmd-11-4843-2018

Wu, K., Palmer, P. I., Wu, D., Jouglet, D., Feng, L., & Oda, T. (2023). Theoretical assessment of the ability of the MicroCarb satellite city-scan observing mode to estimate urban CO2 emissions. *Atmospheric Measurement Techniques*, *16*(2), 581–602. https://doi.org/10.5194/amt-16-581-2023

Wu, K., Yang, D., Liu, Y., Cai, Z., Zhou, M., Feng, L., & Palmer, P. I. (2023). Evaluating the ability of the pre-Launch TanSat-2 satellite to quantify urban CO2 emissions. *Remote Sensing*, *15*(20), 4904. https://doi.org/10.3390/rs15204904

Wunch, D., Toon, G. C., Blavier, J.-F. L., Washenfelder, R. A., Notholt, J., Connor, B. J., et al. (2011). The total carbon column observing network. *Philosophical Transactions of the Royal Society A: Mathematical, Physical & Engineering Sciences*, *369*(1943), 2087–2112. https://doi.org/10.1098/rsta.2010.0240

Yadav, V., Ghosh, S., Mueller, K., Karion, A., Roest, G., Gourdji, S. M., et al. (2021). The impact of COVID-19 on CO2 emissions in the Los Angeles and Washington DC/Baltimore metropolitan areas. *Geophysical Research Letters*, *48*(11). https://doi.org/10.1029/2021GL092744

Yadav, V., & Michalak, A. M. (2013). Improving computational efficiency in large linear inverse problems: An example from carbon dioxide flux estimation [Software]. *Geoscientific Model Development*, *6*(3), 583–590. https://doi.org/10.5194/gmd-6-583-2013

Yañez, C. C., Hopkins, F. M., Xu, X., Tavares, J. F., Welch, A., & Czimczik, C. I. (2022). Reductions in California's urban fossil fuel CO_2 emissions during the COVID-19 pandemic. *AGU Advances*, *3*(6). https://doi.org/10.1029/2022AV000732

Zazzeri, G., Graven, H., Xu, X., Saboya, E., Blyth, L., Manning, A. J., et al. (2023). Radiocarbon measurements reveal underestimated fossil CH_4 and CO_2 emissions in London. *Geophysical Research Letters*, *50*(15). https://doi.org/10.1029/2023GL103834

References From the Supporting Information

Hong, S.-Y., Noh, Y., & Dudhia, J. (2006). A new vertical diffusion package with an explicit treatment of entrainment processes. *Monthly Weather Review*, *134*(9), 2318–2341. https://doi.org/10.1175/MWR3199.1

Mesinger, F., DiMego, G., Kalnay, E., Mitchell, K., Shafran, P. C., Ebisuzaki, W., et al. (2006). North American regional reanalysis. *Bulletin of the American Meteorological Society*, *87*(3), 343–360. https://doi.org/10.1175/BAMS-87-3-343

Nakanishi, M., & Niino, H. (2006). An improved Mellor–Yamada level-3 model: Its numerical stability and application to a regional prediction of advection Fog. *Boundary-Layer Meteorology*, *119*(2), 397–407. https://doi.org/10.1007/s10546-005-9030-8

National Oceanic and Atmospheric Administration. (1998). Automated surface observing system user's guide. Retrieved from https://www.weather.gov/media/asos/aum-toc.pdf

National Oceanic and Atmospheric Administration: National Centers for Environmental Information. (2023). Integrated global radiosonde archive (IGRA). Retrieved from https://www.ncei.noaa.gov/products/weather-balloon/integrated-global-radiosonde-archive

Niu, G.-Y., Yang, Z.-L., Mitchell, K. E., Chen, F., Ek, M. B., Barlage, M., et al. (2011). The community Noah land surface model with multiparameterization options (Noah-MP): 1. Model description and evaluation with local-scale measurements. *Journal of Geophysical Research*, *116*(D12), D12109. https://doi.org/10.1029/2010JD015139